Pergamon

0956-7151(93)E0098-N

Acta metall. mater. Vol. 42, No. 7, pp. 2387–2400, 1994

0956-7151/94 $7.00 + 0.00

BAIN STRAIN RELAXATION DURING EARLY STAGE DECOMPOSITION OF A HYPER-EUTECTOID CuBe ALLOY

B. CHEONG[1], K. HONO[2] and D. E. LAUGHLIN[1]

[1]Department of Materials Science and Engineering, Carnegie Mellon University, Pittsburgh, PA 15213, U.S.A. and [2]Institute for Materials Research, Tohoku University, Sendai 980, Japan

(Received 20 July 1993; in revised form 9 December 1993)

Abstract—Decomposition of a hyper-eutectoid β (b.c.c.) phase CuBe alloy into the two phase [γ(B2) + α(f.c.c.)] mixture involves composition separation, b.c.c. to B2 atomic ordering and b.c.c. to f.c.c. crystal lattice rearrangement. In this investigation, the relaxation of the Bain transformation strain associated with the b.c.c. to f.c.c. lattice rearrangement is studied by TEM during the early stages of decomposition and experimental findings are interpreted within the framework of an elasticity theory of plate-like precipitates. We have found that relaxation of the Bain strain proceeds gradually with the advancement of decomposition. A decomposition sequence which is consistent with the microstructures is: b.c.c. to B2 ordering → isostructural secondary decomposition and the formation of {001} plate-like G. P. zones (b.c.t.) → b.c.c. to f.c.c. crystal lattice rearrangement and the formation of plate-like α' (f.c.t.) precipitates with {001} habit planes → gradual relaxation to α (f.c.c.) phase. From habit plane stability analysis, we demonstrate that the intermediate α' (f.c.t.) state is elastically unstable. Driven by this instability, the relaxation was found to occur mainly through the interplay of two basic mechanisms, that is, habit rotation and the formation of polytwin morphology. The interplay was manifested in the form of characteristic saw-tooth type polytwin plates. From a careful analysis of as-quenched states, we have found that the formation of the saw-tooth morphology initiates by plate intersection through the formation of stacking faults. We have explained this in terms of a dislocation model.

1. INTRODUCTION

Phase transformations in solids are often accompanied by the rearrangement of crystal lattices. A rearrangement of the crystal lattice of a parent phase into that of a product phase involves a macroscopic shape change or homogeneous distortion of the parent lattice. The Bain distortion that is associated with b.c.c. ↔ f.c.c. crystal lattice rearrangement is a classic example of this. What has proven to be an important question in regard to the crystallography and the morphology of a phase transformation involving a crystal lattice rearrangement is; how is the homogeneous distortion accommodated as it develops? This is a particularly interesting question with regard to diffusional transformations in which a lattice rearrangement accompanies diffusional atomic reconfiguration processes such as atomic clustering and/or ordering.

The situation we are considering is well represented by decomposition reactions which occur in CuBe alloys: decomposition of α (f.c.c.) phase in Cu-rich alloys (f.c.c. → B2 + f.c.c.) and decomposition of β (b.c.c.) phase in Be-rich hyper-eutectoid alloys (b.c.c. → f.c.c. + B2). Both of these reactions involve compositional phase separation, B2 atomic ordering and crystal lattice rearrangement of the b.c.c. ↔ f.c.c. type. Decomposition of Cu-rich α phase has been studied in a number of experimental investigations [1–4]. According to these studies, a supersaturated α phase decomposes into the equilibrium mixture through the following sequence:

$$\alpha \text{ (f.c.c. disordered)} \rightarrow \alpha_1 \text{ (Cu-rich f.c.c.)}$$
$$+ \text{ Be-rich equiaxial G. P. zone}$$
$$\rightarrow \alpha_2 + \text{plate-like G. P. zone} \rightarrow \alpha_3 + \gamma''$$
$$\rightarrow \alpha_4 + \gamma' \rightarrow \alpha_{eq} + \gamma_{eq} \text{ (B2 ordered).}$$

The main focus in this complex decomposition reaction has been placed on the nature of the intermediate γ'' and γ' phases in conjunction with the f.c.c. and b.c.c. (B2) crystal lattice rearrangement. These γ phases were shown to have different crystal lattices distinct from that of the equilibrium γ phase as well as different habit planes belonging to the same zone. Recently, Khachaturyan and Laughlin (K–L) [5] have provided a theoretical account of these experimental findings by use of the elasticity theory [6] of a plate-like precipitate. They have proposed that the intermediate γ phases are elastically constrained states of the same cubic B2 phase whose relative differences are brought about by differences in habit orientation. The results of their calculations are in good agreement with the existing experimental data. Thus diffusional habit plane rotation has been established as an important mechanism of the relax-

ation of transformation strain during decomposition of the α phase.

Unlike decomposition of the α phase, decomposition of β (b.c.c.) phase of hyper-eutectoid composition has not been studied in as much detail and only limited information is available from some early investigations [7–9]. According to the TEM observations made by Tadaki *et al.* [8] and later by Auvray [9], the Bain strain relaxation during β phase decomposition renders microstructures which are far more complicated than those due to the α phase decomposition. This has caused significant discrepancies between interpretations of different experimental studies and quite a few important questions are still left unanswered. In this study, we carry out a TEM investigation in an attempt to establish a better understanding as to how a radical change in crystal structure (b.c.c. to f.c.c.) can be achieved during decomposition of a hyper-eutectoid CuBe alloy. In doing this, we adopt the line of reasoning advanced by K–L [5] for decomposition of α CuBe alloys. It turns out that elasticity is a vital conceptual framework whereon major features of decomposition may be properly understood. During this study, we place our focus exclusively on the early stages of decomposition process, as represented typically by as-quenched states. Due to the remarkably rapid decomposition kinetics of CuBe alloys, many characteristic events occur during the early stages. Therefore, a precise understanding of as-quenched states is very important. We will discuss the strain relaxation during later stages of decomposition in a separate paper [27] on the basis of information which we gain from this study.

2. EXPERIMENTAL

Cu–Be binary alloys containing 9.04 wt%Be (41.2 at.% Be) were furnished by BrushWellman Inc. in the as-cast condition. The as-cast alloys were homogenized for one day at 840°C before they were quenched into water. The quenched alloys were sliced into plates about 0.5 mm thick and were subsequently cold-rolled to thicknesses of about 0.2 mm. Due to the brittleness of specimens, further reduction in thickness was made by mechanical polishing. Discs of 3 mm in dia were punched out from these specimens and were then given a disordering treatment for 1 h at 840°C. For each of these heat treatments, the specimens were encapsulated in argon back-filled quartz tubes. The disordered specimens were quenched into iced-brine water by rapidly transferring a tube and smashing it onto a heavy metal object which was immersed in the quenchant.

Specimens for TEM were prepared using a twin-jet electro-polisher with an electrolyte of 70 vol.% methanols and 30 vol.% nitric acid below -30°C and at 10 V. When necessary, electropolished samples were ion-milled for short periods of time (<10 min) at 4–5 keV and 0.2 mA. Conventional TEM was performed using a Philips 420T microscope operating at 120 kV. High Resolution TEM was conducted with JEOL 4000EX microscope at 400 kV.

3. RESULTS

3.1. Overall characteristics of as-quenched states

The kinetics of decomposition of the hyper-eutectoid CuBe alloy are remarkably fast and the early stages of the decomposition process could not be suppressed by rapid quenching. The overall nature of a typical as-quenched state is shown by a series of photographs in Fig. 1 taken near the [100] zone axis of the ordered γ (B2) matrix phase. From the micrographs, the precipitates are found to be very thin (6–20 Å) plates with their habit plane normals nearly parallel to the $[010]_\gamma$ and $[001]_\gamma$ directions of the ordered γ matrix. Corresponding to this, the precipitate reflections (e.g. spot 1) are elongated along the same directions in the Selected Area Diffraction Pattern (SADP). The streaks around the matrix γ reflections (e.g. spot 2) are presumed to result from double diffraction as well as from thin distorted layers of the matrix adjacent to the broad faces of the precipitate plates.

On close inspection of the Bright Field (BF) image [Fig. 1(b)] and of the Dark Field (DF) image [Fig. 1(d)] taken with a precipitate reflection (spot 1), one can find a characteristic striation contrast inside the precipitate plates. On the other hand, in the Superlattice Dark Field (SDF) image [Fig. 1(c)] taken with a matrix reflection (spot 2), the plates are imaged as dark regions with no striation contrast inside. This suggests that the contrast is not due to thin γ phase regions, as proposed in an early TEM investigation [8] but may be due to planar defects existing inside the precipitate plates. The nature of the defects, however, is not immediately clear from the photographs. It is interesting to note, from the SDF image, that no Antiphase Boundary (APB) contrast is detectable in the ordered γ matrix. Considering that the earliest stages of decomposition may commence with b.c.c. to B2 ordering, one can expect that APB's if they existed at all, may have been consumed by the Cu-rich precipitates. It is not certain, however, whether precipitation on APB's has made a significant contribution to the precipitation on the whole.

The $[100]_\gamma$ zone axis pattern shown in Fig. 2(a) provides more information on the structural aspects of the precipitates. In Fig. 2(b), the zone axis patterns of two precipitate variants are schematically reproduced, being superimposed on the $[100]_\gamma$ zone axis pattern of the matrix γ phase. From the array of precipitate reflections due to one variant, it is found that the *constrained crystal structure* [5, 10] of the precipitate phase is f.c.t. (we will designate f.c.t. as α'). The orientation relationship between the matrix and the α' precipitate is determined to be

$$[100]_\gamma // [110]_{\alpha'} \quad [\bar{1}10]_\gamma // [010]_{\alpha'}$$

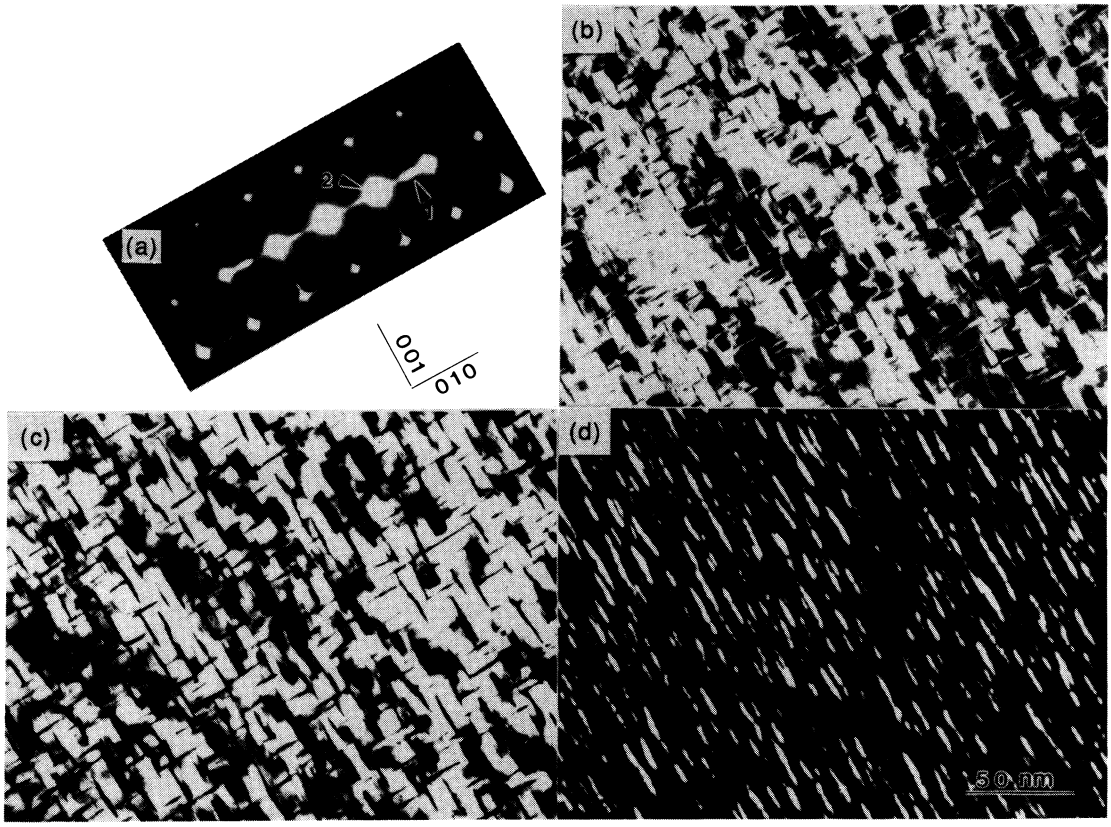

Fig. 1. Overall characteristics of the rapidly-quenched state. (a) SADP taken near the $[100]_\gamma$ zone axis. (b) Associated BF image. (c) DF image taken with the precipitate reflection marked 1 in the SADP. (d) SDF image taken with the matrix reflection marked 2 in the SADP. Notice the arrays of very thin precipitate plates with habit plane normals nearly parallel to $[010]_\gamma$ and $[001]_\gamma$ directions. Notice also the lack of APB contrast from (c) and the striation contrast inside the precipitate plates from (b) and (d).

or

$$(001)_\gamma // (001)_{\alpha'} \quad (001)_\gamma // (001)_{\alpha'}$$

which is the Bain lattice correspondence; the second orientation relationship was attained from the $[\bar{1}10]_\gamma$ zone axis pattern. Considering that the precipitate is coherent with the matrix across the broad face of a plate i.e $a_{\alpha'} = \sqrt{2}a_\gamma$ (a: lattice parameter), we find the tetragonality (t) of the f.c.t. structure to be $t = |\mathbf{g}^\gamma_{002}|/\sqrt{2}|\mathbf{g}^{\alpha'}_{002}| = 0.84$ where $\mathbf{g}$ denotes the diffraction vector in the SADP. This indicates that the α' precipitates in this as-quenched state has already accommodated about one half of the Bain transformation strain.

Characterization of the α' precipitate was first made by Tadaki *et al.* [8] and Auvray [9] in independent TEM investigations. In these works, the precipitate was proposed to be a metastable phase or an intermediate phase, distinguished from the stable equilibrium α(f.c.c.) phase. As we will discuss in detail later, we suggest that the α' precipitates are an elastically unstable transient state which naturally evolves, through the b.c.c. to f.c.c. Bain crystal lattice rearrangement, from plate-like G. P. zones with $\{001\}_\gamma$ habit. This unstable nature of the precipitate leads to a rapid development of the processes which prompt a further relaxation of the Bain strain. In this respect, it is interesting to note from the BF image that the habit planes of many precipitate plates are slightly deviated from the $\langle 001\rangle_\gamma$ directions either globally over a whole plate or segmentwise. In addition, striation contrast is quite noticeable inside the precipitate plates (notice also the associated streak-like intensity in the SADP). Considering that the contrast is due to planar defects which may further the relaxation of the Bain strain, one would expect that they may be either stacking faults or twins.†

With the habit planes rotated and/or planar defects introduced, the crystal lattice of the precipitates is distorted from the α'(f.c.t.) state and is no longer in Bain lattice correspondence. The lattice deformation

†Unlike stacking faults, twins are obviously not planar defects but render them in the form of twin boundaries. For convenience, however, we will use the term "planar defect" when we need to refer to both collectively.

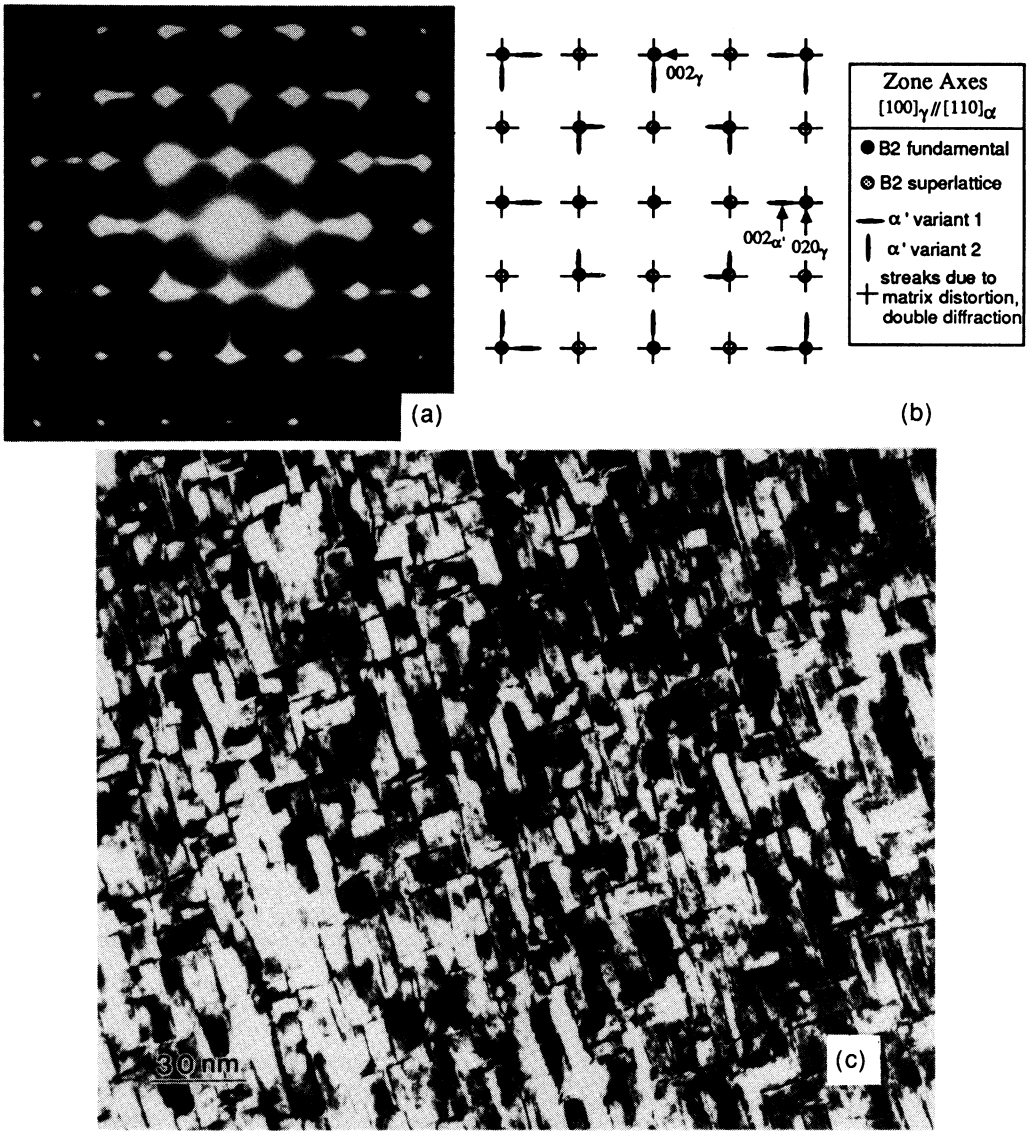

Fig. 2. (a) $[100]_\gamma$ zone axis SADP. (b) Schematic illustration of the basic pattern of the SADP ($[100]_\gamma // [100]_{\alpha'}$). (c) BF image associated with (a). Streak-like intensity distribution associated with precipitate reflections is not reproduced in (b).

may involve not only a change in the lattice constants but also a rotation of the precipitate crystal lattice with respect to that of the matrix. When monitoring such crystal deformation in the reciprocal space, one should be able to see the corresponding changes in direction as well as in magnitude of the reciprocal lattice vectors. Indeed, one can notice from the SADP [Fig. 2(a)] that the precipitate reflections are not sharply elongated but have the shape of a tadpole, in spite of the very thin nature of the precipitate plates. We may best understand the shape by envisaging the head part of a tadpole shape as due to a range of precipitate crystal lattices which have varying degrees of Bain strain relaxation. On this basis, we now examine in more detail the planar defects in the as-quenched alloys.

3.2. Polydomain precipitate plates in as-quenched states

The micrographs shown in Fig. 3(a), and (b) were taken from another quenched specimen. Although the quenching rate was not intentionally varied, the microstructure is rather coarse unlike the ones previously shown. For convenience, we will denote this relatively slower-quenched alloy as Q2 and that of the more rapidly quenched alloys as Q1. From the BF image, one can notice that the majority of the precipitate plates have a characteristic *saw-tooth* morphology [see also Fig. 4(c)]. This morphology is featured by a slight rotation of two broad segments neighboring a thin band (10–30 Å thick) from the $\langle 001 \rangle_\gamma$ direction.

Figure 3(b) shows the DF image taken with the streaked precipitate reflection ($\mathbf{g}^{prec}_{111}$) indicated in the SADP. The most prominent features are found that in each single plate, both thin and broad regions are in opposite contrast and that for each type of region, the contrast reverses between two orthogonal sets of the plates with $\sim\{001\}_\gamma$ habits. This indicates that the crystal lattice of the thin regions is in a different cystallographic orientation from that of the broad regions in the same plate and that the thin regions in one set of plates have a similar crystal lattice orientation as the broad regions in plates of the other set. This is expected for plates containing polytwin domains. Other important features to note are as follows. Firstly, the proportion of the broad and thin regions in a plate is systematic. It is measured to be approximately 4:1. Secondly, all of the thin regions of bright contrast are aligned in the same direction. From rotation calibration, it is found that the plane normal of these thin regions coincides with the direction of the streaking of the precipitate reflection ($\mathbf{g}^{prec}_{111}$).

A $[100]_\gamma$ zone axis pattern taken from the same region of the specimen, is presented in Fig. 4(a). Two characteristic features are readily noticeable and they are marked by arrows: twofold-split distinct

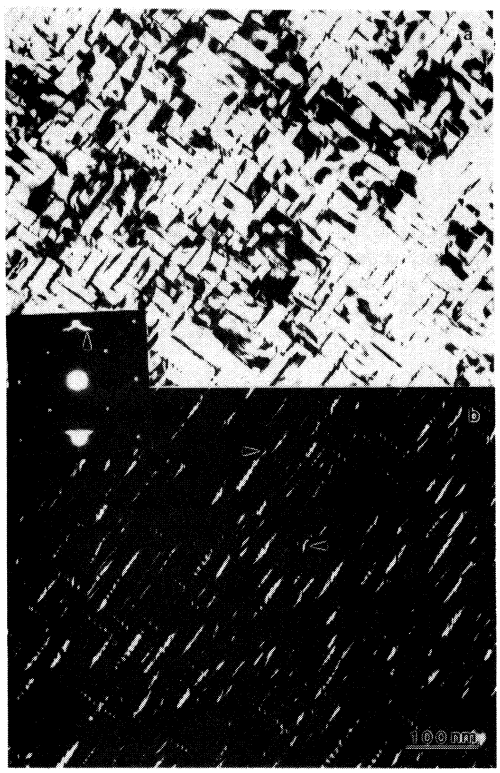

Fig. 3. Microstructure of the Q2 alloy. (a) BF image. (b) DF image taken with the precipitate reflection ($\mathbf{g}^{prec}_{111}$) indicated in the associated SADP. As compared to the case of Q1 alloys (Figs 1 and 2), precipitate plates are noticeably coarser. Majority of precipitate plates display a characteristic saw-tooth morphology [see the schematic in Fig. 4(c)].

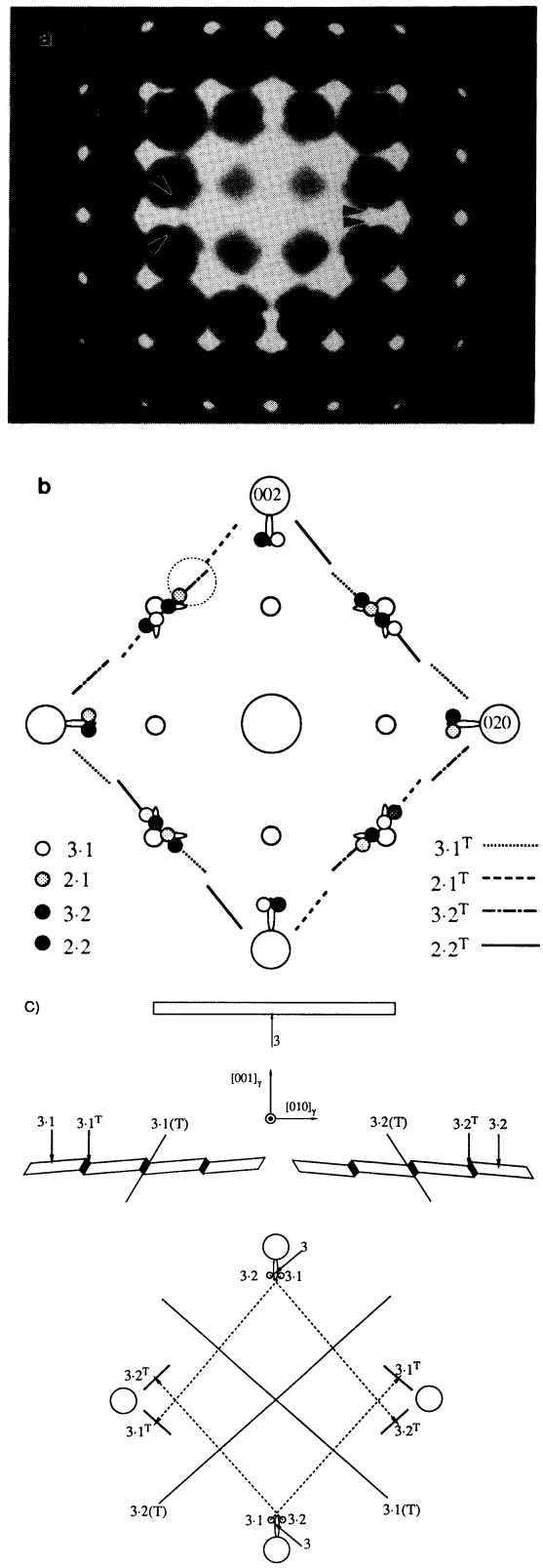

Fig. 4. (a) SADP taken from the same region of the Q2 alloy shown in Fig. 3 along the $[100]_\gamma$ zone axis. (b) Schematic illustrating the constitution of the SADP. (c) Schematic illustrating the origins of the two fold-split distinct precipitate reflections and of the streak-like intensity. Each of these features is marked by arrows in (a).

precipitate reflections and the streak-like intensity near those reflections. The origins of these features are schematically illustrated in Fig. 4(c). In the diagrams, numeric symbols represent orientational variants with each one characterizing a different orientation of the precipitate crystal lattice. For example, $3 \cdot 2^T$ denotes the twin of the second minor orientational variant of the major variant 3: major variants 1, 2 and 3 refer to the precipitate plates whose habit normals were initially parallel to $[100]_\gamma$, $[010]_\gamma$ and $[001]_\gamma$, respectively. The symbols $3 \cdot 1(T)$ and $3 \cdot 2(T)$ denote the twin planes associated with the variants $3 \cdot 1$ and $3 \cdot 2$, respectively. From the schematic diagrams, one can clearly see that broad twin domains are responsible for the twofold-splitting of distinct precipitate reflections and that thin twin domains account for the streak-like intensity. By extending the procedure depicted in Fig. 4(c) to other low order reflections, we constructed the diffraction pattern shown schematiclly in Fig. 4(b). The resulting pattern successfully reproduces most of the salient aspects of the actual SADP. The good agreement beteen the two patterns lends support to the assumption that we used for the construction. That is, $[110]_{prec}//[100]_\gamma$ remains an invariant axis during the rotation of the segment habit and hence of the precipitate crystal lattice as the precipitates relax from the α' state by the formation of polytwin domains. With the aid of the schematic SADP [Fig. 4(b)], we may now clearly understand the contrast in DF image of Fig. 3(b). That is, imaging of the precipitate refelctions within the encircled area of Fig. 4(b) by DF should produce bright contrast for the domains due to $2 \cdot 1$ and $3 \cdot 2^T$ ($2 \cdot 1$ denotes major domains in the plates rotated 90° clockwise with respect to the plates containing $3 \cdot 1$).

The interpretation that we made regarding the streak-like intensity due to the thin twin regions enables us to distinguish it from the streak-like intensity due to the other type of planar defects, that is, stacking faults. As shown in Fig. 5 by enlarged views, the streak-like intensity in Fig. 2(a) differs in both positions and directions from the one due to thin twin regions in Fig. 4(a). The schematic diagram presented in Fig. 6 illustrates this point [compare with Fig. 4(c)]. Figure 7 shows BF and DF images which were taken from an as-quenched state similar to that of Fig. 2 (i.e. Q1) by use of the same diffraction condition as that of Fig. 3. It should be noted from the DF image that in comparison with the DF image of Fig. 3(b), the contrast due to thin twin domains is now virtually absent in the plates of the variant $3 \cdot 2$. A few of the detectable thin twin domains are marked by arrows. Consistent with this finding, the striation contrast prevailing in the plates of the variant $3 \cdot 1$ appears to be type 2 contrast rather than the contrast related to the saw-tooth morphology. This suggests that for the as-quenched state Q1, streak-like intensity and associated striation contrast

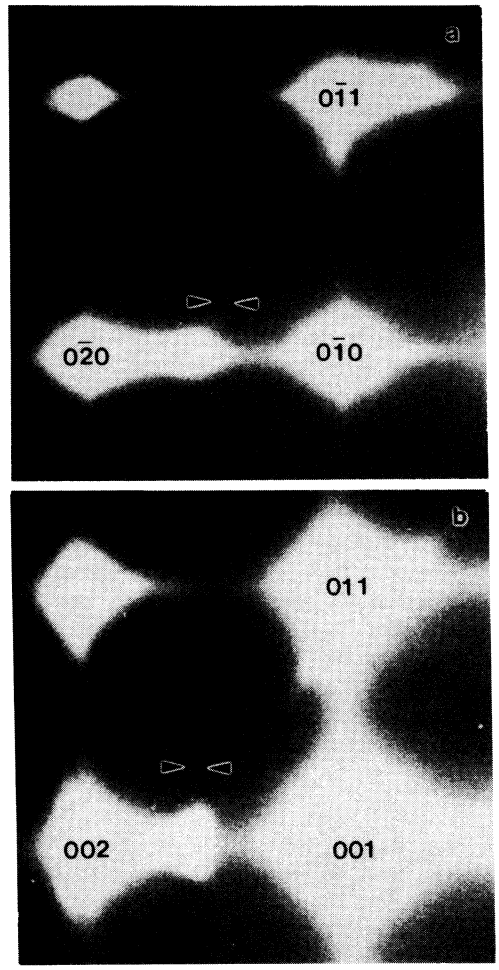

Fig. 5. Comparison between two different kinds of streak-like intensity. (a) Enlargement of a section in Fig. 2(a). The streak-like intensity is due to stacking faults. (b) Enlargement of a section in Fig. 4(a). The streak-like intensity is due to thin twin domains. Notice that the streak-like intensity in (a) differs in both position and direction from the one in (b). Compare (a) and (b) with Fig. 6 and Fig. 4(c), respectively.

may be ascribed not to thin twin domains but to stacking faults.

From the foregoining characterization of the poly-domain (poly-twin domain and poly-translational domain or stacking faults) plates in two different as-quenched alloys, a few fundamental questions arise; "what are the possible mechanisms of formation?" and "do different polydomain plates form via different mechanisms?". With regard to these questions, a close examination of Fig. 3 in relation to Fig. 7 leads to a few interesting observations. A prominent feature, as commonly observed in both as-quenched states, is the intersection of plates. To be more specific, plates of one orientation are often intersected by plates of another orientation and in such cases, the intersecting plate is always found connected with a planar defect in the plate intersected. This can be seen, for example, near the

locations indicated by arrows in Fig. 3(b) and in Fig. 7(a). Another feature to note is; as the average size of the plates increases from one quenched state to another, the predominant planar defects change from stacking faults to twin domains (i.e. the width of planar defects increases). From these observations, the following suggestions may be offered. Firstly, intersection of plates may play an important role in the formation of either stacking faults or twin domains in an initially single domain plate. Secondly, the formation of twin domains may initially start with the formation of stacking faults through shearing process but the overall kinetics of formation may be diffusion-controlled. According to this view, the stacking faults in more rapidly quenched Q1 alloys are kinetically arrested features of the developing twin domains and thus may be regarded essentially as embryonic or underdeveloped twin domains.

3.3. High Resolution TEM (HRTEM) study of an as-quenched (Q1) state

In the foregoing, we characterized the planar defects in the precipitate plates of the as-quenched alloys based on conventional TEM. Although this characterization, on its own, is self-consistent, the extremely fine nature of the defects still makes a direct visual evidence desirable, especially in view of the controversy in existing interpretations. In previous TEM studies, the possibility of planar defects being "quasi-eutectic γ phase" [38] or stacking faults [39] was suggested, as opposed to our interpretation. In order to clarify this and to gain information which may either support or help us detail the proposed outline of a possible formation mechanism, high resolution TEM was carried out for the as-quenched state comparable to that of Fig. 7 (i.e. Q1 alloy).

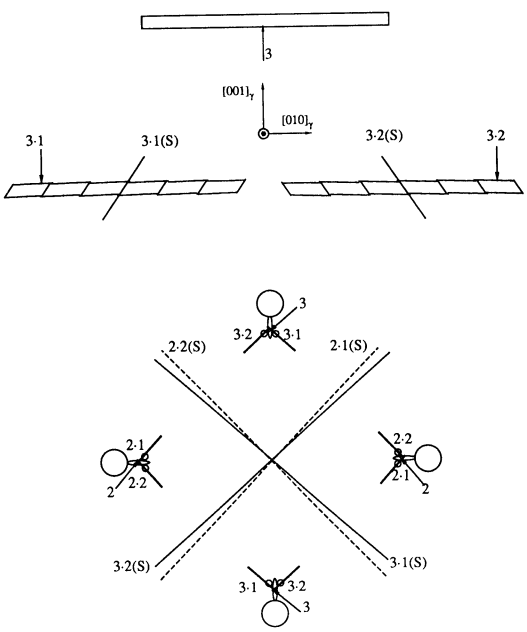

Fig. 6. Schematic illustrating the streak-like intensity due to stacking faults in Fig. 2(a) and in Fig. 5(a).

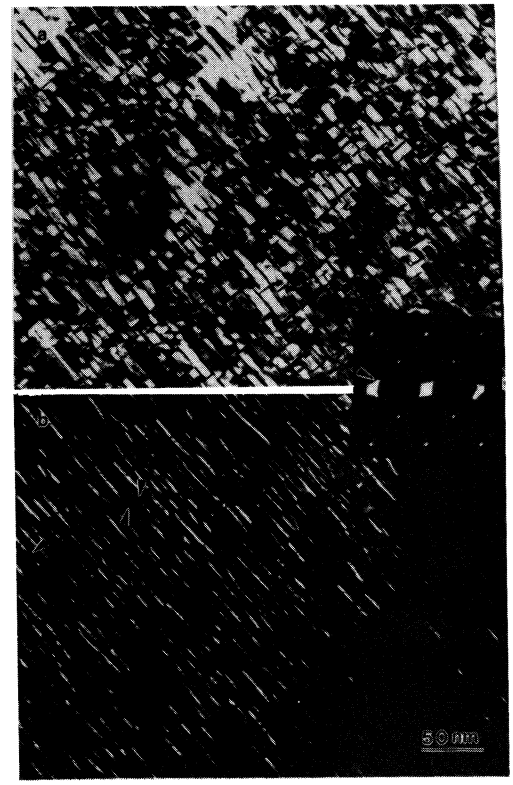

Fig. 7. TEM micrographs taken from the Q1 as-quenched state by use of the same diffraction condition as that of Fig. 3(b). (a) BF image. (b) DF image. Notice that thin twin domains are now virtually non-existent in the plates of the variant 3 · 2. A few of the detectable thin twin domains are marked by arrows in (b).

Figure 8 shows a many-beam lattice image taken exactly along the $[100]_\gamma$ zone axis. The $[110]_{prec}$ axis is nearly parallel to this direction. By virtue of the enhanced resolution, one can clearly see a strong correlation between the intersection of plates and the formation of planar defects. In this regard, it is interesting to note that the average distance between planar defects is quite comparable to the interspacing between plates. Although intersecting plates are not detectable near some of the planar defects, this does not rule out the possible role of plate intersection in the formation of the planar defects. This point may be illustrated, for example, by the feature marked "1". The feature, together with a noticeable non-uniformity in size and thickness of the precipitate plates suggest that the absence of intersecting plates may be mainly due to the dissolution of the plates during the coarsening process which is already under way. This may explain why intersecting plates were not frequently observed near thin twin domains in the relatively slow-quenching state shown in Fig. 3. Where intersecting plates are observed, it is found that a plate is intersected at its broad face by either a plate of the other orientation from one side, or by

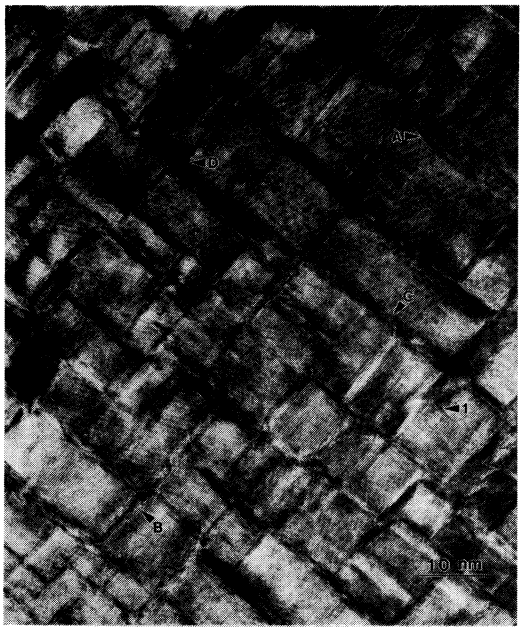

Fig. 8. Many beam lattice image taken along $[100]_\gamma // [110]_{prec}$. Notice a strong correlation between the intersection of plates and the formation of planar defects.

two plates, one from either side. One may be interested to notice that in the latter case, two intersecting plates are often shifted relative to each other along the broad face of an intersected plate and connected to a planar defect. It seems to be obvious that conjugation of the second intersecting plate is not likely to occur without being mediated by the existing planar defect. This is because the intersection of each plate on either side of a broad face is most probably a diffusionally isolated event, which may not lead to a correlation in their intersecting positions.

Figure 9 presents an enlarged view of the regions marked A in Fig. 8. Near the upper broad face of the precipitate, one can notice the continuity of lattice planes, indicating that the interface is highly coherent. What appears to be planar defects in Fig. 8 are marked by arrows. Although the precise nature of defects can not be determined due to blurriness of the atomic column images, it is clear that there are lattice disturbances. Near these defects, the precipitate unit cells are slightly more elongated along the thickness direction with some monoclinicity. In conjunction with this, they are also slightly rotated relative to the unit cells away from defects (for example, see the atomic columns indicated by two solid lines). This explains the origin of the tadpole shape of the precipitate reflections which we indicated in Fig. 2. Planar defects marked B and C in Fig. 8 are shown in Fig. 10(a, b), respectively. Each of these planar defects is associated with a single intersecting plate.

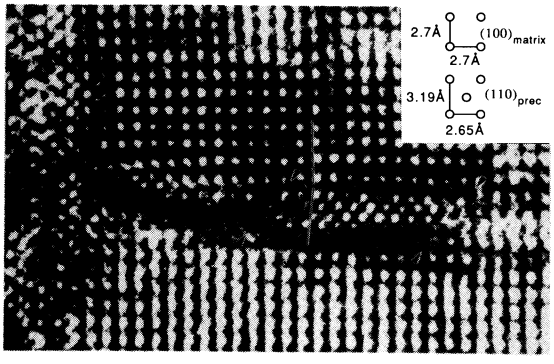

Fig. 9. Atomic resolution image of the region marked A in Fig. 8. Notice that near the defects marked by arrows (whose nature is not exactly known), precipitate unit cells are not only more elongated along the thickness direction but also rotated relative to the unit cells away from defects.

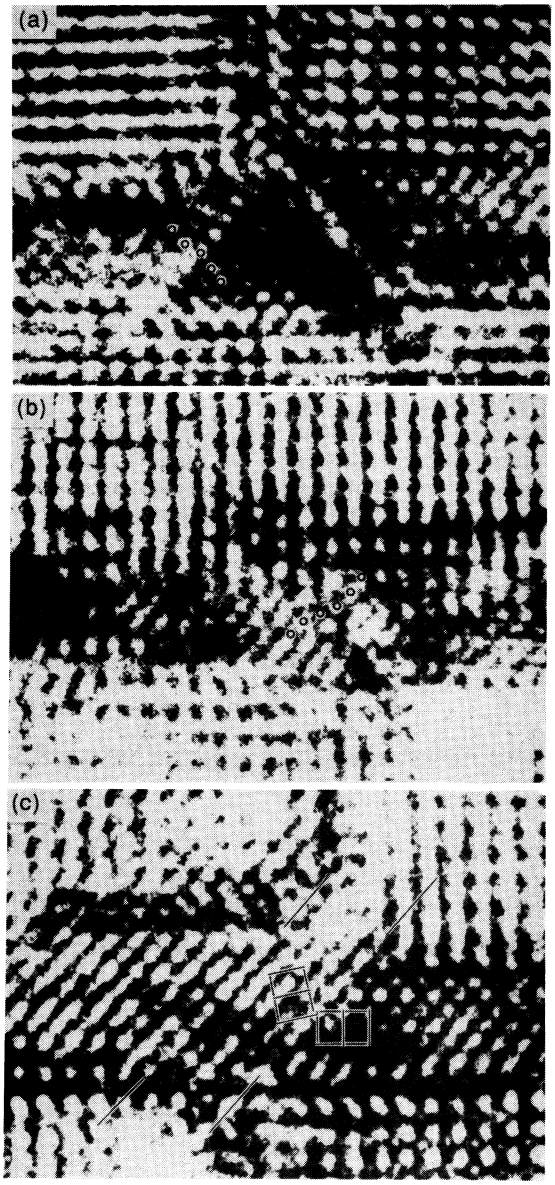

Fig. 10. Atomic resolution images of the planar defects marked by B, C and D in Fig. 8. (a) B; intrinsic stacking fault. (b) C; extrinsic stacking fault. (c) D, twin.

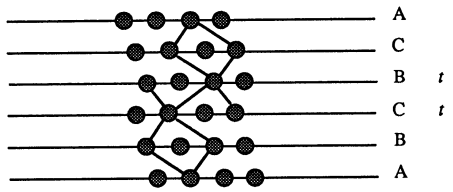

a) Intrinsic Stacking Fault

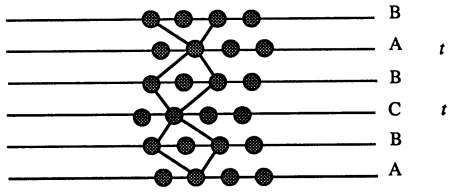

b) Extrinsic Stacking Fault

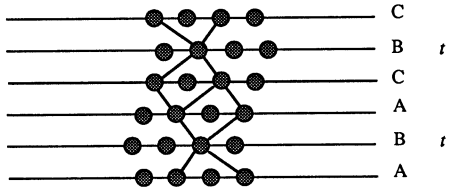

c) Twin

Fig. 11. Schematic illustrating the (111) stacking sequence in various planar defects. Notice that the number of twinned layers in each type of planar defect is (a) 2, (b) 3 and (c) minimum 4. t denotes the mirror plane of a local stacking sequence.

In the micrographs, circles superimposed on certain atomic columns represent the stacking sequence of (111) planes across each planar defect. By comparison with the schematic diagram shown in Fig. 11, these planar defects are found to be stacking faults; presumably intrinsic (B) and extrinsic (C). A planar defect associated with two intersecting plates (feature marked D in Fig. 8) is shown in Fig. 10(c). One can clearly notice a thin twin region of a unit cell width. We consider that these results of Fig. 10 may not be taken as an indication that two intersecting plates are required for the formation of a twin domain. Rather, they could be taken as a suggestion that given the kinetics, the formation of a twin domain may be facilitated by the association of the two intersecting plates.

The high resolution images shown in Figs 8–10 also render important information regarding the mechanism of early stage decomposition. In discussing the lack of APB contrast in the SDF image of Fig. 1(c), we considered the possibility of the precipitation of Cu-rich precipitates on APB's. If precipitation on APB's were a prevailing decomposition mechanism, an anti-phase shift in the atomic columns of the matrix phase should be frequently observed across a precipitate plate in the high resolution images. Instead, we find from Figs 9 and 10 that the atomic columns on opposite sides of each plate are in-phase. A careful examination of Fig. 8 also led to a consistent observation of this in-phase relation except for a few precipitate plates. Providing that b.c.c. to B2 ordering has preceded the precipitation, this indicates that the average APD size resulting from the ordering was too large for the precipitation on APB's to be a dominant mechanism.

4. DISCUSSION

4.1. Early stage decomposition path and the Bain strain relaxation

As initially noted by Tadaki *et al.* [8] and Auvray [9], the earliest stages decomposition of the hyper-eutectoid β phase have a rapid kinetics and a conventional water-quenching always leads to the formation of two phase microstructures which consist of the B2 ordered phase and Cu-rich coherent plate-like precipitates with average habit planes close to $\{001\}_\gamma$. The overall morphology of the microstructure is typical of an isostructural decomposition in a cubic alloy except for some striation contrast inside the precipitate plates. From this as well as from phase diagram characteristics of the hyper-eutectoid alloys, we are led to presume that the earliest stages of decomposition of the β phase may proceed as follows:

(1) b.c.c. to B2 ordering;
(2) isostructural decomposition leading to the formation of $\{001\}_\gamma$ Cu-rich G. P. zones;
(3) crystal lattice rearrangement of $\{001\}_\gamma$ G. P. zones into $\{001\}_\gamma$ α' (f.c.t.) precipitates;

The thermodynamic and kinetic origins of the suggested decomposition path and the Bain strain relaxation along this path, are now discussed.

In Fig. 12(a), a portion of the CuBe phase diagram [12] is schematically reproduced with relevant lines added and/or extrapolated. The critical line of the second order A2 $\rightarrow$ B2 ordering transition is depicted as a dashed line. It is shown to form a critical end point [13] at which $\beta/(\beta+\gamma)$ and $\beta/(\gamma+\gamma')$ two phase boundaries intersect with the line of A2 $\rightarrow$ B2 ordering. The dotted lines demarcate the *conditional spinodals* in which spinodal decomposition is thermodynamically possible contingent upon A2 $\rightarrow$ B2 ordering [14–17]. As the temperature decreases, a branch of the spinodal lines merges into the line of A2 $\rightarrow$ B2 ordering [10, 17] as shown in the diagram. Figure 12(b) represents a chemical free energy vs composition diagram which is consistent with the phase diagram characteristics at an arbitrary temperature T_a below the eutectoid point. The free energy of the γ(B2) phase plotted in the diagram is assumed to be such that for a given composition, it satisfies the extremization condition: $(\partial F/\partial \eta)|_c = 0$. According to the diagrams, a disordered β phase of the composition c^β, if supercooled to the temperature

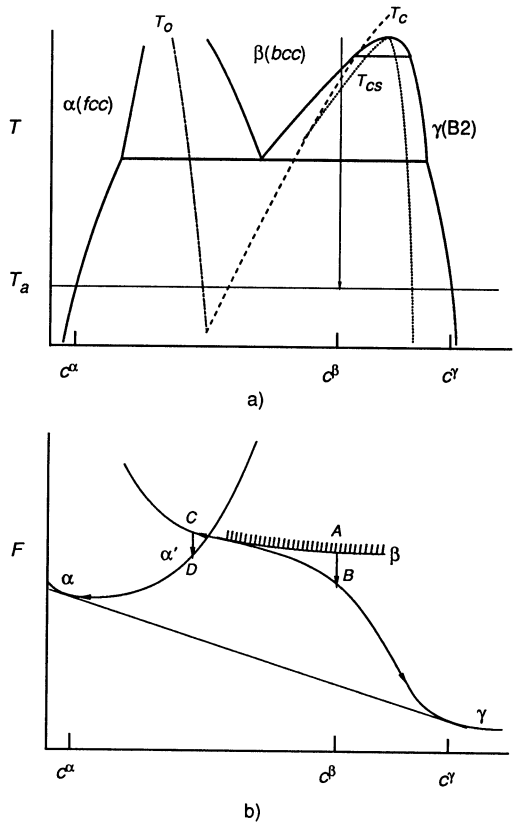

Fig. 12. (a) Schematic of the CuBe phase diagram (See text). (b) Chemical free energy vs composition diagram consistent with the phase diagram characteristics at an arbitrary temperature T_a. When supercooled to T_a, a disordered β phase of the composition c^β, would decompose along the path A → B → C → D to produce the α' (f.c.t.) precipitates.

T_a, would decompose along the path A → B → C → D to produce the α' precipitates.

4.1.1. Congruent ordering: A → B. Being unstable with respect to the fluctuations of long range order, the disordered phase transforms to the homogeneous B2 ordered phase without change in composition (*congruent ordering*). Since there is no need of long range volume diffusion, the kinetics of this process is thought to be extremely fast. Using hypo-eutectoid and eutectoid β phase alloys (eutectoid composition: 5.11 wt%Be or 31.5 at.%Be), Tyapkin *et al.* [18, 19] and Auvray [9] examined the earliest stages of decomposition. By virtue of the extended stability (or metastability) of the β phase in these alloys, they were able to observe the initial ordering reaction. Based on diffraction studies, it was suggested that the disordered β phase initially orders to the metastable Cu_2Be (β'') ordered phase. We believe that the Cu_2Be type ordering would not occur in hyper-eutectoid alloys, particularly in alloys of compositions far from the eutectoid composition. This is because the Cu_2Be structure is a non-special point ordered structure in the b.c.c. lattice. Unlike a special point ordered structure, the stability of a non-special point structure depends strongly on the change in interatomic potential with composition and temperature, and hence results in a very limited region of stability (or metastability) in the T–c diagram [10, 20].

4.1.2. Isostructural secondary decomposition: B → C. The non-stoichiometric B2 ordered phase resulting from the congruent ordering is unstable with respect to long wave concentration fluctuations because it lies inside the region of the conditional spinodal. When the average APD size of the B2 phase is much larger than the wave length of the concentration fluctuations (which appears to be our case), this would lead to a continuous phase separation of the B2 ordered phase by the spinodal mechanism: in the presence of a large density of APB's, the spinodal mechanism may not represent a viable path due to inherent kinetic advantage of precipitation on APB's [14, 21–23].

As a consequence of the isostructural secondary decomposition, Cu-rich $\{001\}_\gamma$ plate-like G. P. zones form within the Be-enriched B2 matrix. The plate shape and the $\{001\}_\gamma$ habit of the G. P. zones are a manifestation of the minimization of the elastic strain energy which is associated with the difference in composition-dependent lattice parameters between the G. P. zones and the matrix B2 phase.† It is emphasized that the crystal lattice of the G. P. zones is no longer cubic but is tetragonally elongated along the direction of the habit plane normal since it is subject to the coherency constraint along the $\{001\}_\gamma$ habit planes. This is shown by equation (1) which is derived from equation (A7) (see Appendix)

$$\frac{a(3)_{\text{G.P.}}}{a(1)_{\text{G.P.}}} \cong \frac{a(3)_{\text{G.P.}}}{a(1)_\gamma} = 1 + \epsilon_0\left(1 + \frac{2C_{12}}{C_{11}}\right) \qquad (1)$$

where $a(1)$ and $a(3)$ denote the constrained lattice parameters along [100] and [001] directions, respectively and ϵ_0 is the stress free dilatational strain defined by

$$\epsilon_0 = \frac{da}{a\,dc}(c_{\text{G.P.}} - c_\gamma), \qquad (2)$$

where c denotes the Cu concentration. Due to the lack of necessary data [i.e. composition-dependent lattice parameters and elastic constants of b.c.c. (or B2) phase], an estimation of equation (1) could not be made. It may suffice to point out that this tetragonal elongation of the G. P. zone lattice relieves, in effect, the Bain strain which will result from the b.c.c. (or B2) to f.c.c. crystal lattice rearrangement of the following stages.

4.1.3. Crystal lattice rearrangement: C → D. The {001} G. P. zones resulting from the secondary decomposition undergo the Bain crystal lattice

†According to the estimation made in [5], the elastic anisotropy of B2 phase is negative ($C_{11} - C_{12} - 2C_{44} < 0$ where C_{ij}'s are the Voigt notation of elastic constants), and thus {001} habit plane is stable

rearrangement, as they continue to be enriched in Cu content. Being subject to the coherency constraint, this transition leads to the α' (f.c.t.) precipitates with $\{001\}_\gamma$ habit planes. The tetragonality of the constrained lattice of the α' precipitates is derived from equation (A7) to be

$$\frac{a(3)_{\alpha'}}{a(1)_{\alpha'}} \cong \frac{a(3)_{\alpha'}}{\sqrt{2}a(1)_\gamma} = \frac{1}{\sqrt{2}}\left(1 + \epsilon^0_{33} - \frac{2C_{12}}{C_{11}}\epsilon^0_{11}\right) \quad (3)$$

where $a(1)$ and $a(3)$ denote the constrained lattice parameters along [100] and [001] directions of the precipitate lattice, respectively and ϵ^0_{11}, ϵ^0_{33} are the stress free transformation strains defined by

$$\epsilon^0_{11} = \frac{a_\alpha - \sqrt{2}a_\gamma}{\sqrt{2}a_\gamma}, \quad \epsilon^0_{33} = \frac{a_\alpha - a_\gamma}{a_\gamma} \quad (4)$$

where a's denote the lattice parameters of the stress free α and γ phases with compositions of α' and γ phases. An estimation of equation (3) was made by use of the lattice parameters of the f.c.c. pure Cu crystal ($a = 3.612$ Å) and equilibrium B2 phase ($a = 2.7$ Å) and elastic constants of the pure Cu ($C_{11} = 1.684 \times 10^{12}$ dyne/cm^2 and $C_{12} = 1.214 \times 10^{12}$ dyne/cm^2). This gives $a(3)_{\alpha'}/a(1)_{\alpha'} = 0.89$, which is about 6% larger than the tetragonality value ($=0.84$) measured from Fig. 2(a).† Within the context of the theory used, this discrepancy can be ascribed directly to the use of the lattice parameters for $c_{\alpha'} = 1$ and $c_\gamma = 0.5$, that is to say, an upper bound condition. This, in turn, suggests that the composition of the precipitates shown in Fig. 2(a) remains different from that of the equilibrium state.

4.2. Instability of the α′ state and subsequent relaxation

The α' precipitate which has the $\{001\}_\gamma$ habit plane inherited from the $\{001\}_\gamma$ G. P. zone is unstable with respect to further relaxation of the Bain strain. This can be demonstrated by the use of the habit stability condition which was derived in [24]. It predicts that a plate-like precipitate with $\{001\}_\gamma$ habit plane is unstable if the following condition is met

$$\frac{\epsilon^0_{33}}{\epsilon^0_{11}} < 1 + \frac{\xi}{2}\left(1 + \frac{2C_{12}}{C_{11}}\right) \quad (5)$$

where

$$\xi = \frac{C_{11} - C_{12} - 2C_{44}}{C_{44}}.$$

The right hand side of the equation has the absolute minimum value ($=-2$) in the limiting case of $C_{12} \to C_{11}$. This establishes a useful criterion, namely that a plate-like precipitate the $\{001\}_\gamma$ habit plane is elastically unstable regardless of elastic constants, if $\epsilon^0_{33}/\epsilon^0_{11} < -2$. Estimation of the $\epsilon^0_{33}/\epsilon^0_{11}$ ratio by use of the lattice parameter of pure Cu and that of the equilibrium B2 phase gives $\epsilon^0_{33}/\epsilon^0_{11} = -6.25$, which is much smaller than the minimum value for the stability.

As a consequence of the instability of the α' state, further relaxation of the Bain transformation strain immediately sets in, contingent upon transition of the $\{001\}_\gamma$ G. P. zone to the α' state. As we have shown in Section 3, this involves the formation of the polytwin plates of a saw-tooth morphology.

4.3. Formation mechanism of the polytwin plate of a saw-tooth morphology

In understanding the formation mechanism of the saw-tooth type polytwin plates, one may need to address the following questions: (1) How do twin domains nucleate? (2) How do twins grow and how is their growth related to the segment-wise habit rotation? (3) What are the atomic mechanisms responsible for segment-wise habit rotation? To answer these questions completely is a daunting task since it necessarily involves scrutiny of related fundamental issues in the studies of diffusionless and of diffusional phase transformations. In the following, we limit our attention and attempt to answer the first question on the basis of the most consistent observation we have made from the microstructures of the as-quenched alloys, that is, the intersection of the plates. We have suggested earlier that the intersection of plates plays an important role in nucleation of twin domains through the formation of stacking faults.

The $(100)_\gamma$ cross section of two intersecting $\langle 001\rangle_\gamma$-oriented α' (f.c.t.) precipitate plates, is schematically depicted in Fig. 13. In the diagram, the tetragonality of the α' precipitates is taken to be 0.83 and all the indices are given with respect to the variant 3 crystal lattice which is in Bain correspondence with the matrix lattice (upper and lower crystals are taken to be variant 2 and variant 3, respectively). As one can notice from the atomic configuration near the boundary between two variants, an immediate consequence of the impingement of a variant 2 plate with the broad face of a variant 3 plate is the generation of a *quasi* misfit dislocation. The local Burgers vector [25] of the dislocation is defined to be $\mathbf{b} = (a'/2)[\bar{1}10]$ according to the **SF**/*RH* convention depicted in the diagram. As opposed to the conventional misfit dislocations which often reside at stable matrix/precipitate interfaces as an agent of misfit accommodation, the resulting dislocation has the following characteristic: it is subject to a highly strained environment in which the variant 3 crystal is elastically unstable and ready to relax the Bain strain. Under these circumstances, the dislocation may dissociate by the following reaction to produce a mobile Schockley partial which can

†It is emphasized that the measured tetragonality value is not referred precisely to the $\{001\}\alpha'$ state but to a near $\{001\}\alpha'$ state in which the Bain strain relaxation is also achieved by introduction of stacking faults. The contribution from the stacking faults, however, would be probably very small in view of their sparse density.

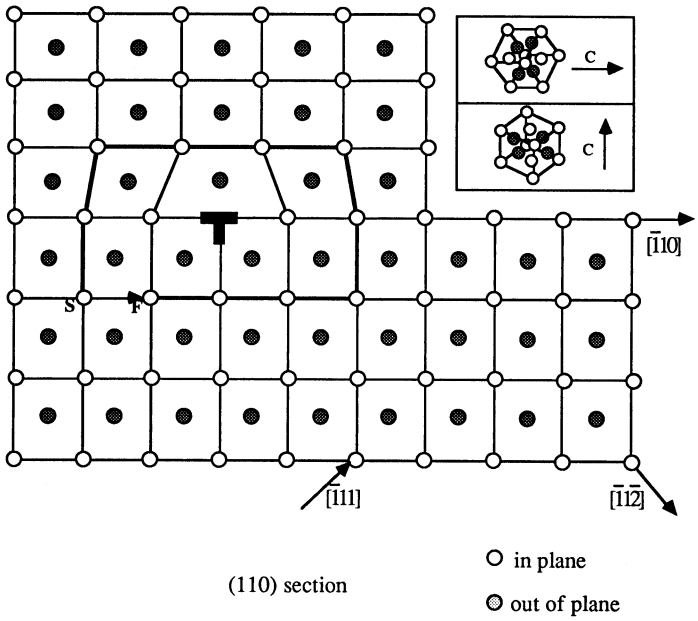

Fig. 13. Schematic illustrating the generation of a quasi-misfit dislocation as a consequence of impingement of a variant 2 plate (upper crystal) with the broad face of a variant 3 plate (lower crystal). The dislocation dissociates to produce a mobile Shockley partial which then glides to create an intrinsic stacking fault on the ($\bar{1}$11) plane.

then glide to create an intrinsic stacking fault on the ($\bar{1}$11) plane

$$\frac{a'}{2}[\bar{1}10] \rightarrow \frac{a'}{3}[\bar{1}11] + \frac{a'}{6}[\bar{1}\bar{1}2]. \tag{6}$$

It is noted that the number of stacking faults due to a plate intersection depends on thickness of the impinging variant 2 plate. For example, when the variant 2 plate is as thick as of ten $(001)_{var2}$ planes, two intrinsic stacking faults may be created with the average interval of six $(\bar{1}11)_{var3}$ planes. By a slight extension of the model, one can expect that an extrinsic fault may be produced when two thin plates of the variant 2 impinge on the variant 3 plate with one from either side.

Whether the described dislocation reaction can actually occur is thought to depend primarily on the elastic stress field inside the variant 3 precipitate plate. When perturbation due to impingement of the variant 2 plate is neglected, this means that the homogenous stress field of the variant 3 plate should be able to provide the resolved shear stress which at least can overcome the resisting force associated with the creation of a stacking fault, i.e. $\tau > \gamma/b$ where τ, γ and b are the resolved shear stress, the stacking fault energy and the magnitude of the Burgers vector, respectively. By use of equation (A1), a general expression of the elastic stress tensor may be written as

$$\sigma_{ij} = -C_{ijkl}(\epsilon^{t}_{kl} - \epsilon^{0}_{kl}) \tag{7}$$

where ϵ^{t}_{kl} is the tensor of the total homogeneous strain, given by equation (A2) and (A3). For the variant 3 plate with the habit plane normal $\mathbf{n} = [001]_{\gamma}$, equation (7) is reduced to

$$\hat{\sigma} = \begin{pmatrix} \sigma_{11} & 0 & 0 \\ 0 & \sigma_{11} & 0 \\ 0 & 0 & 0 \end{pmatrix} \tag{8}$$

where

$$\sigma_{11} = -C_{11}\epsilon^{0}_{11}\left(1 + \frac{2C_{12}}{C_{11}}\right)\left(1 - \frac{C_{12}}{C_{11}}\right). \tag{9}$$

Since ϵ^{0}_{11} is negative in the case we are considering, the plate is in a planar tensile stress state with no stress component along the habit plane normal. The resolved shear stress on the $(\bar{1}11)_{\alpha'}$ plane along the $[\bar{1}\bar{1}2]_{\alpha'}$ direction (nearly parallel to $(011)_{\gamma}$ and $[01\bar{1}]_{\gamma'}$ respectively) is then approximately $\tau \approx 0.5\,\sigma_{11}$. Evaluation of τ leads to $\tau \approx 3 \times 10^{10}$ dyne/cm^2. From the stacking fault energy of Cu ($\gamma \approx 78$ erg/cm^2) [26] and $b \approx 10^{-8}$ cm, the minimally required resolved stress is estimated to be $\tau_{min} \approx 8 \times 10^{9}$ dyne/cm^2. From this, a conclusion is reached that intersection of plates and the ensuing dislocation reaction of equation (6) are responsible for the nucleation of a twin domain (or formation of a stacking fault).

With regard to how stacking faults grow into twin domains, we presently have little understanding and it needs to be readdressed in a carefully designed separate investigation. Within the limitation of our present work, it may suffice to discuss briefly in what direction the answer is supposed to lie. We consider that it may be very difficult to account for growth of

a twin domain exclusively in terms of diffusionless atomic motion, i.e. conservative dislocation motion. According to our calculation [27], a polytwin plate with the (001) habit plane, is supposed to have twin domains of about 20% in volume fraction. In view of the extreme rapidity of dislocation motion, this means that, even in rapidly-quenched alloys, one would be able to observe the polytwin plates with nearly the predicted volume fraction of twin domains, if only diffusionless atomic motion were responsible. Instead, we observed the predominant existence of stacking faults in Q1 alloys.† It is also very unlikely for a twin domain to grow via diffusional atomic motion alone, particularly inside an existing plate and in the presence of a mobile twinning dislocation. In light of this discussion, a possible mechanism might be one which involves non-conservative as well as conservative motion of the twinning Schockley partial dislocation which participated in the nucleation of a twin domain. To be more specific, the Schockley partial dislocation, unable to cross-slip, may advance to the next $(\bar{1}11)$ plane by climb to add another layer of the stacking fault by glide motion. This alternating process of glide and climb motion does not appear to be unreasonable, given a relatively high reaction temperature and a finite climb force due to the stress field inside the precipitate plate (existence of the climb force can be clearly seen by the use of the Peach–Koehler equation [25]).

5. CONCLUSIONS

The Bain transformation strain relaxation during early stage decomposition of the hyper-eutectoid Cu–9.0wt%Be alloy was studied by TEM and the experimental findings were interpreted within the framework of the elasticity theory of a plate-like precipitate. The results are summarized as follows:

1. Accommodation of the Bain transformation strain proceeds gradually with the advancement of decomposition. A decomposition sequence which is consistent with the observed microstructrues is suggested to be: b.c.c. to B2 ordering → isostructural secondary decomposition and subsequent formation of the {001} plate-like G. P. zones (b.c.t.) → b.c.c. to f.c.c. crystal lattice rearrangement and formation of the plate-like α' (f.c.t.) precipitates with {001} habit planes → gradual relaxation to α (f.c.c.) phase.
2. We have shown that the intermediate α' precipitates are elastically unstable, which prompts further Bain strain relaxation contingent upon transition from the plate-like G. P. zone state. The relaxation process involves formation of characteristic saw-tooth type polytwin plates by nucleation and growth of twin domains inside the existing $\langle 100\rangle_\gamma$-oriented single domain plates and by concomitant segment-wise habit rotation.
3. From a careful characterization of as-quenched states using conventional TEM and HRTEM, we have shown that the formation of the saw-tooth morphology initiates by plate intersection through the formation of stacking faults. A dislocation model was proposed to explain nucleation of a twin domain.

†In addition to a few other aspects which we do not specify here, a pole mechanism [28, 29], a widely accepted dislocation mechanism of deformation twinning in f.c.c. crystals, seems to be unsatisfactory in this aspect. According to Cottrell and Bilby's estimation [28], it takes only a few nanoseconds for a single atomic twinned layer to grow by a pole mechanism.

Acknowledgements—We are thankful to Professor A. G. Khachaturyan for his interest in our study and for helpful discussions and to Professor J. M. Howe of University of Virginia for his help on the High Resolution TEM study. We also gratefully acknowledge the BrushWellman Inc. for a fellowship and for providing the CuBe alloys.

REFERENCES

1. A. H. Geisler, J. H. Mallery and F. E. Steigert, *Trans. Am. Inst. Min. Engrs* **194,** 307 (1952).
2. K. Shimizu, Y. Minakami, H. Mitani and K. Otsuka, *J. Japan Inst. Metals* **34,** 1108 (1970).
3. V. A. Phillips and L. E. Tanner, *Acta metall.* **21,** 441 (1973).
4. R. J. Rioja and D. E. Laughlin, *Acta metall.* **28,** 1310 (1980).
5. A. G. Khachaturyan and D. E. Laughlin, *Acta metall. mater.* **38,** 1823 (1990).
6. A. G. Khachaturyan, *Sov. Phys. Solid St.* **8,** 2163 (1967).
7. M. I. Zakharova and Ye. M. Amosov, *Fizika Metall.* **14,** 599 (1962).
8. T. Tadaki, T. Sahara and K. Shimizu, *Trans. Japan Inst. Metals* **14,** 401 (1973).
9. X. Auvray, Sc. D. thesis, Univ. Rouen, France (1977).
10. A. G. Khachaturyan, *Theory of Structural Transformations in Solids.* Wiley, New York (1983).
11. S. H. Wen, A. G. Khachaturyan and J. W. Morris Jr, *Metall. Trans.* **12A,** 581 (1981).
12. D. J. Chakrabarti, D. E. Laughlin and L. E. Tanner, *Bull. Alloy Phase Diagr.* **8,** 269 (1987).
13. S. M. Allen and J. W. Cahn, *Bull. Alloy Phase Diagr.* **3,** 787 (1982).
14. S. M. Allen and J. W. Cahn, *Acta metall.* **24,** 425 (1976).
15. H. Ino, *Acta metall.* **26,** 827 (1978).
16. H. Kubo and C. M. Wayman, *Metall. Trans.* **10A,** 633 (1979).
17. H. Kubo and C. M. Wayman, *Acta metall.* **28,** 395 (1980).
18. Y. D. Tyapkin and V. A. Golikov, *Phys. Met. Metall.* **35,** 336 (1973); **36,** 1058 (1973).
19. V. A. Golikov and Y. D. Tyapkin, *Phys. Met. Metall.* **37,** 322 (1974).
20. A. G. Khachaturyan, *Progress in Materials Science* (edited by B. Chalmers, J. W. Christian and T. B. Massalki), Vol. 22, p. 150. Pergamon Press, Oxford (1978).
21. R. Z. Abdulov, V. I. Syutkina and O. D. Shashkov, *Fizika Metall.* **45,** 118 (1978).
22. D. V. Sukhanov, T. S. Boyarshinova and O. D. Shashkov, *Fizika Metall.* **68,** 316 (1989).
23. Long-Qing Chen and A. G. Khachaturyan, *Acta metall. mater.* **39,** 2533 (1991).

24. B. Cheong, Ph.D. thesis, Chaps 2, 5 and Appendix, Carnegie Mellon Univ., Pittsburgh (1992).
25. J. P. Hirth and J. Lothe, *Theory of Dislocations*, McGraw-Hill, New York (1968).
26. L. E. Murr, *Interfacial Phenomenon in Metals and Alloys*. Addison-Wesley, Reading, Mass. (1975).
27. B. Cheong, K. Hono and D. E. Laughlin, *Metall. Trans.* **24A,** 2605 (1993).
28. A. H. Cottrell and B. A. Bilby, *Phil. Mag.* **42,** 573 (1951).
29. J. A. Venables, *Phil. Mag.* **6,** 379 (1961).

APPENDIX

Crystal Geometry of a Constrained Plate-like Precipitate

According to elasticity theories of a plate-like precipitate [6, 10], the total homogeneous strain that is experienced by a thin coherent plate-like precipitate embedded in an anisotropic infinite matrix is given by equation (A1) and equation (A2) for the habit plane normal $\mathbf{n}_0$

$$\epsilon^{t}_{ij} = \epsilon^{0}_{ij} + \epsilon_{ij} \tag{A1}$$

$$\epsilon^{t}_{ij} = \frac{1}{2}(S_i n^{0}_{j} + S_j n^{0}_{i}) \tag{A2}$$

where ϵ^{t}_{ij}, ϵ^{0}_{ij} and ϵ_{ij} are the tensors of total homogeneous strain, stress free transformation strain and elastic strain, respectively and S_i is the ith component of the shear vector $\mathbf{S}$ specified by

$$\mathbf{S} = \hat{\Omega}(\mathbf{n}_0)\hat{\sigma}^0\mathbf{n}_0 \tag{A3}$$

$\hat{\Omega}$ and $\hat{\sigma}^0$ are defined by

$$\sigma^{0}_{ij} = \lambda_{ijkl}\epsilon^{0}_{kl} \tag{A4}$$

$$\Omega^{-1}_{ij} = \lambda_{ijkl} n^{0}_{k} n^{0}_{l} \tag{A5}$$

where λ_{ijkl} is the elastic modulus tensor. Since the total deformation includes the rigid body rotation to maintain the continuity of the crystal lattice across the interphase

$$u^{t}_{ij} = S_i n^{0}_{j} = \frac{1}{2}(S_i n^{0}_{j} + S_j n^{0}_{i}) + \frac{1}{2}(S_i n^{0}_{j} - S_j n^{0}_{i}) = \epsilon^{t}_{ij} + \omega_{ij} \tag{A6}$$

where the symmetric (ϵ^{t}_{ij}) and the antisymmetric (ω_{ij}) part describe the total homogeneous strain and the rigid body rotation, respectively. With the total deformation $\{u^{t}_{ij}\}$ known, the geometry of the crystal lattice of a constrained precipitate is completely determined using the relation

$$\mathbf{R}^{p} = \hat{\mathbf{A}} \cdot \mathbf{R}^{m} = (\hat{\mathbf{I}} + \hat{\mathbf{u}}) \cdot \mathbf{R}^{m} = (\hat{\mathbf{I}} + \mathbf{S}\mathbf{n}_0) \cdot \mathbf{R}^{m} \tag{A7}$$

where $\hat{\mathbf{A}}$ is the transformation matrix and $\mathbf{R}^{p}$, $\mathbf{R}^{m}$ are lattice vectors of the precipitate and the matrix lattice referred to the same reference coordinate system.